

1
2
3
4
5
6
7
8
9
10
11
12
13
14
15
16
17
18
19
20
21
22
23
24
25
26
27
28
29
30
31
32
33
34
35
36
37
38
39
40

A deep learning-based approach for high-throughput hypocotyl phenotyping

Orsolya Dobos^{1,2}, Peter Horvath³, Ferenc Nagy¹, Tivadar Danka^{3*}, András Viczián^{1*}

Author affiliations:

1. Institute of Plant Biology, Biological Research Centre of the Hungarian Academy of Sciences, Temesvári krt. 62, H-6726 Szeged, Hungary
2. Doctoral School in Biology, Faculty of Science and Informatics, University of Szeged, Szeged, H-6726, Hungary.
3. Institute of Biochemistry, Biological Research Centre of the Hungarian Academy of Sciences, Temesvári krt. 62, H-6726 Szeged, Hungary

Short title:

Deep learning for high-throughput phenotyping

One-sentence summary:

A deep learning-based algorithm provides an adaptable tool for determining hypocotyl or coleoptile length of different plant species.

Keywords:

plant phenotyping, Arabidopsis, computer vision, machine learning, deep learning

Author contributions:

O.D., T.D., P.H., F.N. and A.V. conceived the original research plans; O.D. performed the experiments; A.V. supervised the experiments, T.D. developed the algorithm; F.N. commented on the manuscript, O.D., T.D. and A.V. analysed the data and wrote the article with contributions of all the authors.

Funding Information:

O.D., A.V. and F.N. were supported by grants from the Economic Development and Innovation Operative Program (GINOP-2.3.2-15-2016-00001 and GINOP-2.3.2-15-2016-00015) and from the Hungarian Scientific Research Fund (OTKA, K-132633). T.D. and P.H. acknowledge support from the HAS-LENDULET-BIOMAG and from the European Union and the European Regional Development Fund GINOP-2.3.2-15-2016-00026.

***Authors for Contact:**

Tivadar Danka: tdanka@brc.hu
András Viczián: aviczian@brc.hu

41 **Abstract**

42 Hypocotyl length determination is a widely used method to phenotype young seedlings. The
43 measurement itself has advanced from using rulers and millimetre papers to assessing
44 digitized images but remains a labour-intensive, monotonous and time-consuming
45 procedure. To make high-throughput plant phenotyping possible, we developed a deep
46 learning-based approach to simplify and accelerate this method. Our pipeline does not
47 require a specialized imaging system but works well with low-quality images produced with
48 a simple flatbed scanner or a smartphone camera. Moreover, it is easily adaptable for a
49 diverse range of datasets not restricted to *Arabidopsis* (*Arabidopsis thaliana*). Furthermore,
50 we show that the accuracy of the method reaches human performance. We not only provide
51 the full code at <https://github.com/biomag-lab/hypocotyl-UNet>, but also give detailed
52 instructions on how the algorithm can be trained with custom data, tailoring it for the
53 requirements and imaging setup of the user.
54

55 **Introduction**

56 Monitoring different aspects of seedling development requires determining certain physical
57 dimensions of the plantlet. Among these, measurement of hypocotyl length is a key
58 phenotypic trait to monitor and quantify different responses. Hypocotyl cells are formed in
59 the embryo and their eventual number set after only a few cell divisions. During seedling
60 growth, the length of the hypocotyl is determined by no further cell divisions but by the
61 elongation of hypocotyl cells (Gendreau et al., 1997). Hypocotyl growth is regulated by a
62 complex network of external and internal factors. Different hormones (auxins, ethylene,
63 cytokinins, abscisic acid, gibberellins and brassinosteroids) are involved in the response
64 (Vandenbussche et al., 2005; Hayashi et al., 2014). Among external cues, gravity not only
65 determines the direction of growth (away from the soil surface) but also affects the hypocotyl
66 elongation (Soga et al., 2018). Our knowledge about how light regulates hypocotyl
67 elongation is much more detailed. Without light, etiolated plants develop elongated
68 hypocotyls, whereas light triggers photomorphogenic development with characteristic,
69 fluence rate-dependent inhibition of hypocotyl elongation, which is one of the key features of
70 the so-called photomorphogenic growth (Fankhauser and Casal, 2004; Arsovski et al.,
71 2012). The role of different light-sensing molecules (photoreceptors) has been revealed in
72 this response: phytochrome B (phyB) is the dominant photoreceptor in red (R), phyA in far-
73 red (FR) and cryptochrome 1 and 2 in blue (B) light (Lin et al., 1996; Nagy and Schäfer,
74 2002). Photomorphogenic ultraviolet B (UV-B) radiation also induces inhibition of hypocotyl
75 elongation (Kim et al., 1998) involving pathways controlled by UV RESISTANCE 8 (UVR8)
76 UV-B receptor (Favory et al., 2009). Fluence rate response curves are used to depict
77 hypocotyl length change over broad light fluences, demonstrating the involvement of
78 specific receptors and their signalling partners in the examined responses. Temperature is
79 the third external cue affecting hypocotyl length. It was recently shown how lower
80 temperature shortens hypocotyl length via phyB in light (Jung et al., 2016; Legris et al.,
81 2016; Casal and Qüesta, 2018).
82 These examples show that hypocotyl length is a seedling phenotypic trait of particular
83 importance. On one hand it indicates the functionality of the examined signalling pathway(s),
84 and on the other hand it is relatively easy to measure, generating quantified data of the
85 observed response. Thus researchers measure hypocotyl length (i) to compare the effect of
86 different light, hormone, etc. treatments, (ii) to analyse the role of signalling components

87 using mutants and overexpressor lines and (iii) to perform different reverse and forward
88 genetic (screening) approaches.
89 The methodology of the hypocotyl measurement has changed over time. In early studies
90 hypocotyls were simply measured by hand one-by-one using a ruler or millimetre paper, in
91 many cases rounding the observed value to the nearest millimetre (Köhler, 1978; Liscum
92 and Hangarter, 1991; Pepper et al., 2001; Dieterle et al., 2005). A more precise and most
93 widely applied quantification procedure involves the arrangement of seedlings on sticky
94 surfaces or agar plates, subsequent scanning or photographing and measurement of
95 hypocotyl length using a digital image processing software (Young et al., 1992; Borevitz and
96 Neff, 2008; Ádám et al., 2013; Das et al., 2016). This approach gives the opportunity to
97 store hypocotyl images and measure them at a later time while involving other
98 experimenters in the measurement procedure. To speed up this process and reduce the
99 invested work-time, different applications have been created to automate the quantification
100 of hypocotyl length (Sangster et al., 2008; Wang et al., 2009; Cole et al., 2011; Spalding and
101 Miller, 2013). These image processing tools have the potential to replace error prone and
102 labour intensive manual image processing and to advance plant phenotyping by enabling
103 high-throughput data analysis. A cornerstone of these algorithms is the plant segmentation,
104 that is, the separation of the plant from the background. This is a difficult task due to the
105 diversity of images, which can be caused, for example, by different image acquisition setups
106 and conditions. However, good segmentation is key to downstream analyses, such as
107 object boundary detection and midline tracking (Spalding and Miller, 2013). In addition to
108 overall plant segmentation, fully automated identification of different plant subparts, such as
109 cotyledons, roots and seedcoats, is a significant challenge, which has not been solved
110 reassuringly in the previous efforts. For hypocotyl length measurement, a major difficulty is
111 the localization of hypocotyl-root junction and robust identification of the cotyledons. Tools
112 based on classical segmentation algorithms have troubles identifying these parts for several
113 reasons, including high variance in phenotypes, variable imaging conditions or noisy
114 images. Since imaging methods are very different from lab to lab and no gold standard is
115 available, it is essential to provide a data analysis pipeline which works robustly for a
116 diverse set of images.

117

118 Up until the recent introduction of deep convolutional neural networks (CNN), a robust
119 image analysis pipeline was extremely difficult to achieve. In contrast to classical methods,
120 modern deep convolutional networks can surpass human performance in many image
121 processing tasks, including object classification and detection (Geirhos et al., 2018). Instead
122 of relying on hand crafted filters and features, a neural network learns the optimal
123 representation of the data. This makes its performance exceptionally good, and given
124 enough data, a well-trained neural network can generalize for a wide range of datasets. For
125 plant phenotyping, these developments have yielded advances in trait identification and
126 genotype/phenotype classification (Pound et al., 2017; Namin et al., 2018).

127

128 In this paper, we present a deep learning-based approach which is able to provide
129 quantified seedling phenotype data in a high-throughput manner. Compared to earlier tools,
130 ours is fully-automated and achieves human expert accuracy on length measurement tasks
131 for various plant species, such as *Arabidopsis* (*Arabidopsis thaliana*), mustard (*Sinapis alba*)
132 and stiff brome (*Brachypodium distachyon*). The method does not require expensive
133 imaging setups, and accurate results can be obtained with a simple flatbed scanner or a
134 smartphone camera. In addition, the measurement itself requires only a few seconds per

135 image, thus reducing the time spent by several orders of magnitude. We provide full access
136 to our algorithm as it is open source and also give detailed instructions how to perform
137 training for customised hypocotyl length determination approaches.
138

139 **Results**

140 **The architecture of the algorithm**

141 To extract the length data from images, first we perform segmentation, followed by the
142 skeletonization of the segmented objects to be measured (Fig. 1A). In the case of a typical
143 seedling, each image is segmented into three non-overlapping parts: 1) background 2)
144 hypocotyl 3) non-hypocotyl seedling area. (The latter category differs between species, thus
145 different non-hypocotyl parts should be defined accordingly.) Central to our approach is the
146 U-Net deep CNN for segmentation, which is particularly excellent for finding thin objects. It
147 has been applied on various problems with success, such as detecting cell nuclei in
148 microscopic images or identifying subparts of the brain on MRI scans (Ronneberger et al.,
149 2015; Buda et al., 2019). U-Net is able to identify specific parts of the plants in images and
150 separate them from the background. On a provided image, U-Net applies convolution
151 operations with various filters followed by maximum pooling repeatedly, producing the
152 segmentation masks. The major difference, as opposed to classical image processing
153 algorithms, is that the filters used by the network are not given in advance but learned from
154 the data during the so-called training phase. In this phase, the segmentation masks
155 provided by the expert are shown for the algorithm several times, which is then able to learn
156 how to classify each pixel either as background or as a specific plant organ. This training
157 process gives rise to filters which are best suited for the task and data, resulting in an
158 extremely robust and adaptable method.
159

160 After the specific plant parts are segmented and identified, the binary images of all identified
161 hypocotyls are skeletonized (Lee et al., 1994). Skeletonization is the reduction of binary
162 shapes to 1 pixel-wide representations, a curve in the case of hypocotyls. This operation
163 allows the length measurement of spatial objects. On the skeleton image, components
164 representing hypocotyls were measured by calculating the number of pixels for each
165 identified object and then converted from pixel unit to *mm*. Pixel to *mm* calculations were
166 performed by either scaling directly with the DPI (dots-per-inch) value of the image or using
167 a reference object on each image. After the measurement, very small objects, which are
168 most likely due to segmentation errors, are filtered out. Finally, the obtained results are
169 exported as an RGB image (Fig. 1B) and a csv file, ready for downstream analysis.
170

171 **The choice of the convolutional network architecture**

172 In general, a CNN repeatedly performs convolutional, pooling and in some instances, batch
173 normalizing operations, eventually extracting a feature-level representation of the image.
174 This is called encoding. During this part, information is compressed and can be lost during
175 the pooling steps. For tasks such as image classification, this is not a problem (Pound et al.,
176 2017). However, for semantic segmentation tasks, the network is required to reconstruct the
177 pixel-level segmentation mask, which is achieved by upsampling the feature-level
178 representation. In this decoding step, the information lost during encoding cannot be
179 recovered and will result in suboptimal results for small or thin objects, such as hypocotyls in
180 our case. This problem was solved with the introduction of U-Net (Ronneberger et al.,
181 2015), originally created to find cells in microscopic images where the cells can grow on

182 each other, having only a thin (occasionally 1-2 pixel wide) region separating them. This is
183 achieved by storing the intermediate feature-level representations before each pooling in the
184 encoding step, then feeding this data to the corresponding upsampling layer. Ever since its
185 inception, U-Net has become a state-of-the-art architecture for semantic segmentation.
186 Because of its performance on small or thin objects, this choice of architecture was ideal for
187 our purposes. To add a regularizing term and accelerate training speed, we have added
188 batch normalizing layers after convolutional blocks (Ioffe and Szegedy, 2015).

189

190 **Phenotypic analysis of Arabidopsis seedlings**

191 Determining hypocotyl length of Arabidopsis seedlings is a key phenotyping procedure in
192 myriads of studies; thus it was obvious to test our algorithm on this model plant first. We
193 simply grew seedlings on wet filter papers under different fluences of monochromatic light
194 sources, laid them on agar plates, scanned them and then used these images to train the
195 algorithm. Altogether we annotated about 2500 hypocotyls and corresponding non-
196 hypocotyl plant parts during this procedure. To test the trained algorithm, we grew seedlings
197 under different fluences of monochromatic R light as a routine treatment for phytochrome
198 studies. Fig. 2A and Supplemental Fig. S1 show how the algorithm recognized long and
199 short hypocotyls belonging to those plants which grow under low or high fluences of light,
200 respectively. The fluence rate graph plotting of the measured hypocotyl length values
201 demonstrates that the algorithm determined values similar to the human experimenters (Fig.
202 2B). To further test the versatility of the algorithm we analysed hypocotyls of seedlings
203 grown in FR and B light when the inhibition of hypocotyl elongation is mediated by phyA and
204 cryptochrome photoreceptors, respectively. Additionally we analysed etiolated seedlings
205 grown in darkness, which are used as important controls in photobiological studies. We
206 found the performance of the algorithm is comparable to humans under these conditions,
207 and the measurement works well even with pale, almost colourless etiolated seedlings
208 (Supplemental Fig. S2, Fig S3, Fig. S4, Fig S5). It was tempting to further examine
209 seedlings which have completely different body architecture. For this purpose, we grew
210 plantlets on plant medium containing sugar with white light illumination. These seedlings
211 have thick hypocotyls, fully developed and opened green cotyledons and long roots. Our
212 results show that the algorithm is capable of measuring the hypocotyls of seedlings grown
213 under light/dark cycles or under continuous white light supplemented with or without
214 photomorphogenic (non-damaging) UV-B irradiation (Supplemental Fig. S6 and Fig. S7).

215

216 **Application of the algorithm on different plant species**

217 To test the usability of our algorithm on other species besides Arabidopsis, we chose
218 mustard (*Sinapis alba*). *Sinapis alba* was an experimental object widely used a few decades
219 ago to examine the dependency of hypocotyl elongation on different irradiation protocols.
220 These works revealed the basic mechanisms of phytochrome action many years before
221 identifying the involved molecular pathways or even the genes coding the photoreceptors
222 (Schopfer and Oelze-Karow, 1971; Wildermann et al., 1978a; Wildermann et al., 1978b). A
223 recent study demonstrates that determining the hypocotyl elongation of *Sinapis alba*
224 seedlings as a phenotypic marker is still in use to monitor hormonal changes under different
225 irradiation conditions (Procko et al., 2014).

226 The *Sinapis alba* plantlets were grown on agar plates under constant white light for 4 days.
227 These seedlings were too bulky to scan them with a flatbed scanner like we did with
228 Arabidopsis seedlings. For this reason, images were taken with a smartphone. We used
229 these images to train our algorithm to identify pixels belonging to *Sinapis alba* hypocotyls

230 and to determine hypocotyl length. During the training phase we annotated about 250
231 hypocotyls and corresponding non-hypocotyl plant parts before performing the presented
232 measurement. Fig. 3 and Supplemental Fig. S8 demonstrate that even low numbers of
233 seedlings were sufficient to train the algorithm and determine hypocotyl length with high
234 accuracy, which is comparable to the performance of human experts.
235 We further tested the versatility of the algorithm by analysing monocotyledonous plants. In
236 monocots, the coleoptile growth is a widely used phenotypic trait instead of the more
237 difficultly observable hypocotyl. We chose stiff brome (*Brachypodium distachyon*), which is a
238 small-sized model plant having a compact and sequenced genome (International
239 Brachypodium Initiative, 2010) and an existing transformation system (Alves et al., 2009).
240 These make it an ideal grass model species with emerging importance (Scholthof et al.,
241 2018). We grew the (*Brachypodium distachyon*) plants under different light fields for 4 days
242 and took photos of them with a smartphone camera. In this case we used 8 images
243 containing about 100 plants to train the algorithm. Fig. 3 and Supplemental Fig. S9 show
244 how the algorithm processed the images and how it measured coleoptile length on the test
245 images. The obtained values do not differ from those measured by the human experts,
246 demonstrating the usability of the algorithm to analyse *Brachypodium distachyon*
247 coleoptiles.

248

249 **Accuracy of the algorithm**

250 To quantitatively assess the performance of our algorithm, we decided to compare the
251 obtained results to the performance of humans. Each measurement was repeated by two
252 human experimenters. For each seedling identified by the algorithm, we calculated
253 measurement accuracy by matching the seedling to the ground truth data provided by the
254 experts (Fig. 4) and calculating the relative error of the measurement. For matching, we first
255 calculated the bounding boxes for each object identified by the algorithm, which is the
256 smallest box containing the segmented object (Fig. 1B). Then the expert provided ground
257 truth segmentation masks were used to check whether there was an actual object in the
258 same spatial location. To see this, bounding boxes of the ground truth masks were also
259 calculated and their position was matched against the position of the algorithm identified
260 object. If a bounding box with at least 10% overlap was found, we matched the two objects
261 and calculated the relative error of the measurement, defined by $|L - M|/L$, where L is the
262 actual length of the hypocotyl (measured by the experts) and M is the result of the
263 measurement (provided by the algorithm). Since the seedlings were placed apart from each
264 other, the possibility of a false matching was minimal. (The 10% overlap criterion was
265 deliberately chosen to be permissive, since requiring larger overlaps essentially guarantees
266 that the relative error is low, thus biasing the accuracy evaluation and masking flaws.) After
267 matching the plants, the false positive (FP) and true positive (TP) ratios were calculated. For
268 a more detailed view on the detection performance, we also calculated the precision and
269 recall values. Precision is defined by $TP/(TP + FP)$, whereas recall was calculated by
270 $TP/(TP + FN)$, with FN denoting the number of false negatives. We calculated accuracy,
271 recall and precision individually for each plant, compared them to the measurement of each
272 expert, then averaged the values. For all of our metrics, a higher value implies a better
273 result (Fig. 4). To put this in perspective, a high precision means that most identified objects
274 are indeed plants (as opposed to segmentation errors), whereas a high recall means that
275 most plants were indeed detected in the image. In general, there is a tradeoff between recall
276 and precision, which is controlled by the strictness of our criteria to accept a match. A too
277 loose criteria lead to an abundance of false detections, resulting in potentially high recall but

278 very low precision. On the other hand, an excessively strict criteria would result in a high
279 false negative rate, leading to low recall and potentially high precision. Thus, the
280 combination of recall and precision together provides a good description on the performance
281 of the algorithm.

282 To obtain further data to characterize the hypocotyl measurement, as the method itself, both
283 human experimenters measured each plant once more, having one month between their
284 two measurements. Using these repeated measurements, we calculated the intra-expert
285 accuracy exactly as we outlined above, using the two measurements provided by the same
286 expert (Fig. 5). The inter-expert accuracy was calculated using the first measurement of
287 both experts. The algorithm performs exceptionally well on plants with long hypocotyls but
288 with slightly lower reliability in case of the very short seedlings grown under strong FR or B
289 light. We also noted that (i) the performance of humans is also poorer when analysing these
290 plantlets both in the case of intra- or inter-expert comparisons (Fig. 5) and that (ii) the
291 algorithm only gives significant difference between groups when the expert measurements
292 also show significant difference according to Student t-test (Fig. S10).

293

294 **Discussion**

295 **Usability of the method**

296 Hypocotyl growth is controlled by the interplay of different external and internal cues, many
297 of them with reciprocal effects. It follows that hypocotyl length is used (i) to characterise
298 activity of numerous signalling pathways, including those controlled by light, hormones,
299 temperature and gravity and that (ii) determination of hypocotyl length is a widely used basic
300 seedling phenotyping assay. Here we report the development of a deep learning-based
301 algorithm to simplify this measurement and save valuable time for the experimenter. There
302 have been computer-based tools published earlier, but here we demonstrate the suitability
303 of deep learning for quantitative plant phenotyping. This method is applicable to a diverse
304 set of image-based phenotyping problems, not restricted to hypocotyl measurement. Our
305 method uses the U-Net CNN architecture for segmentation and can identify not only
306 hypocotyls, but also roots and cotyledons with previously unprecedented detail. To
307 demonstrate the power of the algorithm, we have shown how it performs on other dicot or
308 monocot seedlings. The method possesses several advantages: (i) no image preprocessing
309 is needed; (ii) the algorithm can handle low quality images, i.e. ones made with a simple
310 smartphone camera; (iii) the algorithm works with different imaging conditions; and (iv) its
311 performance matches human accuracy. Moreover, the whole measurement pipeline is semi-
312 automated, and hypocotyl detection and measurement do not require manual intervention at
313 all. This decreases the execution time with several orders of magnitude: while the expert
314 spends 45 minutes on average manually measuring a complete image containing 270
315 seedlings having different hypocotyl length and recording the data, our method performs the
316 same task under a minute. With this speedup, high-throughput assays (testing numerous
317 lines, phenotype-based screenings, etc.) are enabled for a wide array of questions.

318

319 **Assessing our results**

320 To assess the performance of our algorithm, first we focused on Arabidopsis, being the
321 most widely used model plant. Our algorithm performed quite well on seedlings with various
322 body architectures. We tested it on seedlings having short or long, thick or thin hypocotyls;
323 opened or unopened cotyledons with different thickness, size and colour; roots with different
324 length, shape and thickness (Fig. 2 and Supplemental Fig. S1-S7). The accuracy, the

325 precision and recall values, compared to the results of a human experimenter indicate that
326 the algorithm is suitable to replace manual measurements for a wide array of scenarios (Fig.
327 4 and Fig. 5). Our data also show that under specific circumstances, when the plants are
328 short (under strong FR and B light), the accuracy of the algorithm is slightly lower compared
329 to human experimenters. The reasons are quite diverse.

330 (i) The accuracy value is heavily affected by the absolute size of the plant. For example, a 5
331 pixel error on a 100-pixel-long plant has 0.95 accuracy, whereas on a 20-pixel-sized one,
332 the same absolute error yields 0.75 accuracy. (In our images, a typical hypocotyl length of a
333 seedling grown under high light intensities appeared as only approximately 20 pixels.)

334 (ii) In case of short and thick hypocotyls, human experts cannot position their region of
335 interest (ROI) at the middle of the hypocotyl. In this case skeletonization can be different
336 from the human ROI placement.

337 (iii) Misplaced seedlings (hypocotyls touching each other, roots laying over the hypocotyl,
338 etc) or image problems (reflecting plastic plate edges, scratches of the agar surface) disturb
339 the segmentation process but to a lesser extent as with the human experts. These issues
340 can be corrected manually on the generated data, and also a certain carefulness is required
341 during seeding placement onto the agar before the scanning. Another potential source of
342 inaccuracy is the skeletonization of the segmented hypocotyls. Especially for more
343 complicated shapes and cusps, the skeletons may have small additional branches or may
344 not be simply connected at all, which can distort the length measurements.

345 (iv) Especially in the case of seedlings having short and thick hypocotyls, it is not obvious
346 how to define the border between the hypocotyl and the root. For that, images with higher
347 magnification (i.e. microscopy) should be obtained (Fahn, 1990), which is not manageable
348 when working with a high number of seedlings. This problem is a general caveat of the
349 method: the observable morphological traits at the resolution of the scanned images are not
350 sufficient sometimes to mark precisely where the hypocotyl ends and the root begins.

351 Taken together, the inaccuracy generated in these ways is an inevitable component of
352 hypocotyl measurement leading to the errors, not only in case of the algorithm, but also in
353 case of measurements made by humans (Fig. 4 and Fig. 5). Similarly to the algorithm, the
354 expert accuracy also decays when working with small seedlings. However, under these
355 conditions, the expert performance is 10-20% better than the algorithm, although at some
356 points the inter-expert (experts compared to each other) accuracy is not better than the
357 accuracy of the algorithm compared to the experts (Fig. 5). To see if we could improve the
358 accuracy, we trained a new model exclusively on these seedlings and achieved 81%
359 accuracy, 78% precision and 81% recall on the test set. This performance is on par with the
360 experts and points out the importance of the carefully chosen training dataset (Fig S3 and
361 Fig S11). Conclusively, without having solid ground truth data, the training of the algorithm is
362 unavoidably impaired. During the training procedure we annotated about 2500 *Arabidopsis*
363 hypocotyls, whereas annotating approximately 250 *Sinapis alba* seedlings and about 100
364 *Brachypodium distachyon* coleoptiles was sufficient to reach similar recognition metric
365 parameters. These data indicate that *Arabidopsis* is a 'difficult' experimental object in terms
366 of hypocotyl measurement, although we must note that our algorithm trained for *Arabidopsis*
367 is suitable to analyse seedlings with diverse plant architecture, whereas in the case of the
368 two other species we worked with plantlets were grown under only certain conditions.

369

370 **Future outlook**

371 In recent years, the introduction of deep learning and CNNs revolutionized computer vision-
372 based research, making the automation of various tasks and precise high-throughput

373 phenotyping available for many disciplines. In plant biology, several advances have been
374 made with these methods regarding qualitative phenotyping (Pound et al., 2017; Namin et
375 al., 2018; Pineda et al., 2018; Singh et al., 2018; Ramcharan et al., 2019). With these tools
376 however, quantitative phenotypic traits can also be assessed as we demonstrated in this
377 work. The presented segmentation pipeline is not only applicable to length measurements,
378 but in principle it can also be used to measure other parameters, such as cotyledon area,
379 hypocotyl hook opening, angle of cotyledons, etc. With the elimination of manual
380 measurements, the current bottleneck in the phenotyping workflow is the ordered laying of
381 the plantlets onto agar plates with special care to avoid overlaps between the plants. This
382 labour-intensive step can be eliminated using object detection frameworks such as Mask-
383 RCNN (He et al., 2017); however, at present these may cause additional segmentation
384 errors, thus reducing accuracy.

385 While different technical aspects still remain to be overcome, we believe that increasing
386 application and improvement of CNNs for image-based analysis of plants are laying the
387 foundation for the next generation of plant phenotyping tools.

388

389 **Materials and methods**

390 **Code and data availability**

391 The algorithm was implemented in Python, where the PyTorch framework was used for
392 deep learning and the scikit-image library was used for image processing (van der Walt et
393 al., 2014). The code is fully open source and available at GitHub ([https://github.com/biomag-](https://github.com/biomag-lab/hypocotyl-U-Net)
394 [lab/hypocotyl-U-Net](https://github.com/biomag-lab/hypocotyl-U-Net)). Images used for training are also available at
395 <https://www.kaggle.com/tivadardanka/plant-segmentation>. All trained models used in this
396 study are available upon request.

397

398 **Image acquisition and data preparation**

399 *Arabidopsis* (*Arabidopsis thaliana*) seedlings were laid manually onto the surface of 1% w/v
400 agar plates. To ensure optimal algorithm performance, the seedlings were arranged without
401 any overlap. During scanning, a black matte cardboard sheet was used as a reflective
402 document mat. The scanning was done using an EPSON PERFECTION V30 scanner at
403 800 dpi and 24-bit colour setting, and pictures were saved as .tif or .jpg. After the
404 acquisition, hypocotyls, cotyledons, seedcoats and roots were annotated using Fiji
405 (Schindelin et al., 2012). Using the digitizer tablet (WACOM Intuos) instead of a mouse or a
406 touchpad sped up the procedure. The annotated data then were used to create the mask for
407 training the segmentation algorithm. Before training, the images were padded by mirroring a
408 256 pixel-wide strip next to the border. The padded images were cropped up to non-
409 overlapping pieces with 800x800 pixel resolution, which were used to train the neural
410 network. During training, 10% of the images were held out for validation purposes.
411 Experts generated data (Expert 1 and Expert 2) by selecting the midline of the hypocotyls
412 with a single piecewise linear curve, from which the length was measured by ImageJ/Fiji.

413

414 **Training the neural network**

415 To train the U-Net CNN for plant segmentation, about 2500 *Arabidopsis* hypocotyls, 250
416 mustard (*Sinapis alba*) seedlings and 100 stiff brome (*Brachypodium distachyon*) plantlets
417 were annotated. For each of the plant species, a different U-Net model was trained. More
418 details on the U-Net architecture can be found in (Ronneberger et al., 2015). As additional
419 regularization, batch normalization layers were used after the convolutional blocks, which

420 was shown to be highly effective for such CNN architectures (Ioffe and Szegedy, 2015).
421 During training, the smooth Dice coefficient loss was used, introduced by (Milletari et al.,
422 2016; Sudre et al., 2017). The model was trained to classify each pixel as (i) background, (ii)
423 hypocotyl (or coleoptile in the case of *Brachypodium distachyon*) or (iii) plant parts not
424 included in the measurement (root, cotyledon, seedcoat, etc.). The output of the UNet model
425 was an RGB image, where every pixel encoded the probability of belonging to one of the
426 three categories (background: red; hypocotyl (or coleoptile): blue; non-hypocotyl plant parts:
427 green). All connected components of the hypocotyl class were skeletonized, followed by
428 pixel counting. No smoothing function was applied. To assure that the plant parts were
429 precisely segmented, their corresponding term in the loss function was weighted fivefold
430 compared to the background. Training was run for 1000 epochs with initial learning rate $1e-$
431 4 , which was consequently decreased during training to $1e-5$, $1e-6$ and $1e-7$ after epochs
432 200, 600 and 900. The algorithm was trained using a single nVidia Titan XP GPU. For
433 optimization, the Adam optimizer was used (Kingma and Ba, 2014). To prevent overfitting,
434 batch normalization and image augmentation was used. The augmentation transform was
435 composed as a series of random 512x512 pixel crops, affine transforms with flips and a
436 colour jitter transform. The detailed procedure of reproducing the workflow is described as
437 an instructional help document in the Supplemental Method S1-S2. All presented hypocotyl
438 and coleoptile length data were measured on images which were not involved in the training
439 procedure. We recommend the potential users train the algorithm anew using images
440 depicting plants similar to those to be measured and imaged using the same setup.

441

442 **Plant growth conditions and light treatments**

443 *Arabidopsis* (Columbia 0 ecotype) seeds were sown on 4 layers of wet filter paper and were
444 kept at 4 °C for 3 days. To promote homogeneous germination, plates were exposed to 70-
445 $100 \mu\text{mol m}^{-2} \text{s}^{-1}$ white light for 8 h (LUMILUX XT T8 L 36 W/865 fluorescent tubes, Osram),
446 followed by exposure to continuous R ($\lambda_{\text{max}}= 660\text{nm}$), FR ($\lambda_{\text{max}}= 735 \text{ nm}$) or B ($\lambda_{\text{max}}= 470$
447 nm) light for 4 days at 22 °C (SNAP-LITE LED light sources, Quantum Devices). Plates
448 containing dark-grown seedlings plates were wrapped in aluminium foil and kept in dark for
449 4 days at 22°C.

450 Seeds sown on $\frac{1}{2}$ Murashige and Skoog (MS, Sigma-Aldrich) medium containing 1% w/v
451 sucrose and 0.8% w/v agar were surface sterilised and kept at 4 °C for 3 days. Seedlings
452 were grown under 12 h white light ($80 \mu\text{mol m}^{-2} \text{s}^{-1}$)/ 12 h dark photocycles at 22 °C in a
453 growth chamber (MLR-350H, SANYO, Gallenkamp) for 7 days. Alternatively, after 3 days,
454 the plates were placed under continuous white light (PHILIPS TL- D 18 W/33- 640 tubes,
455 $10 \mu\text{mol m}^{-2} \text{s}^{-1}$) supplemented with UV- B (PHILIPS ULTRAVIOLET- B TL20W/01RS
456 tubes, $1.5 \mu\text{mol m}^{-2} \text{s}^{-1}$) for 4 days at 22 °C. The seedlings were covered with transmission
457 cut-off filters (WG series, Schott) using the WG305 filter for UV-B-treated seedlings (+UV-
458 B), and the WG385 filter for the control (-UV-B) seedlings as providing half maximal
459 transmission at 305 or 385 nm, respectively (Bernula et al., 2017).

460 *Brachypodium distachyon* (Bd21) seeds were sown on 1% w/v agar and kept at 4 °C for 5
461 days and were treated with 24 h white light ($130 \mu\text{mol m}^{-2} \text{s}^{-1}$) to induce even germination.

462 Seedlings were grown either in darkness or under $50 \mu\text{mol m}^{-2} \text{s}^{-1}$ R light or $10 \mu\text{mol m}^{-2} \text{s}^{-1}$
463 FR light or $130 \mu\text{mol m}^{-2} \text{s}^{-1}$ white light for 4 days. Subsequently, they were placed on a

464 matte black cardboard sheet and illuminated with even diffused light. Images of the
465 seedlings were taken with a smartphone (iPhone SE, Apple) using the default settings of the
466 camera. Every image contained a millimetre paper for scaling.
467 *Sinapis alba* seeds were sown on 1% w/v agar and kept at 4 °C for 5 days. Seedlings were
468 grown under 130 $\mu\text{mol m}^{-2} \text{s}^{-1}$ white light at 22 °C for 4 days. Seedlings were photographed
469 as described for *Brachypodium distachyon* plants.
470

471 **Acknowledgments**

472 We thank Dr. János Györgyei for providing the *Brachypodium distachyon* seeds and giving
473 advice on seedling propagation. The work was supported by grants from the Economic
474 Development and Innovation Operative Program (GINOP-2.3.2-15-2016-00001, GINOP-
475 2.3.2-15-2016-00015 and GINOP-2.3.2-15-2016-00026) and from the Hungarian Scientific
476 Research Fund (OTKA, K-132633). T.D. and P.H. acknowledge support from the HAS-
477 LENDULET-BIOMAG and from the European Union and the European Regional
478 Development Fund.
479

480 **Supplemental Data**

481 Supplemental Figure S1. U-Net segmentation of red light-grown Arabidopsis seedlings.
482 Supplemental Figure S2. Hypocotyl measurements of Arabidopsis seedlings grown under
483 far-red illumination.
484 Supplemental Figure S3. U-Net segmentation of far-red light-grown Arabidopsis seedlings.
485 Supplemental Figure S4. Hypocotyl measurements of Arabidopsis seedlings grown under
486 blue illumination.
487 Supplemental Figure S5. U-Net segmentation of blue light-grown Arabidopsis seedlings.
488 Supplemental Figure S6. Hypocotyl measurements of Arabidopsis seedlings grown in the
489 dark or under different white light illumination protocols.
490 Supplemental Figure S7. Complete U-Net segmentation of Arabidopsis seedlings grown
491 under white light supplied with photomorphogenic UV-B.
492 Supplemental Figure S8. U-Net segmentation of *Sinapis* plantlets.
493 Supplemental Figure S9. U-Net segmentation of *Brachypodium* plantlets.
494 Supplemental Figure S10. Student t-test p values for testing effect size between groups.
495 Supplemental Figure S11. U-Net segmentation of small far-red light-grown Arabidopsis
496 seedlings, using the model trained on small hypocotyls only.
497 Supplemental Method S1. Creating custom training data.
498 Supplemental Method S2. Training and using the algorithm.
499
500
501

502 **Figures**

503

504 **Figure 1. Overview of the method.**

- 505 (a) Arabidopsis seedlings were placed on agar plate surface and scanned, resulting in
506 the original image. This image was then processed by the previously trained U-Net
507 algorithm (see *Materials and Methods* chapter for details), which determines plant
508 parts: hypocotyls (marked with blue colour) and non-hypocotyl plant parts (depicted
509 by green colour). The background pixels appear in red. This step is called
510 segmentation. During the next step, the algorithm determines a 1-pixel-wide line in
511 the middle of the segmented hypocotyls. This procedure is called skeletonization,
512 and the number of pixels consisting of the 1-pixel-wide lines is proportional to the
513 hypocotyl length. White scale bar represents 1 mm.
- 514 (b) An example of the graphical representation of the algorithm's output. Besides the
515 quantitative parameters of the detected hypocotyls exported to a .csv file, this kind of
516 visualization of the results is also available for the identification of each seedling and
517 for general quality checking of the measurement. The black characters indicate the
518 index of the seedlings in the .csv output (N.1., N.2. etc.) whereas the red numbers
519 show the corresponding hypocotyl length in mm.

520 **Figure 2. Hypocotyl measurement of red light-grown Arabidopsis seedlings.**

- 521 (a) Arabidopsis seedlings were grown on wet filter papers in red light for 4 days, placed
522 on an agar plate and scanned. A close-up image shows a few seedlings grown
523 under high or low fluences of red light and the U-Net segmented and skeletonized
524 images generated from the original by our algorithm. Scale bars represent 1 mm.
- 525 (b) This box-and-whisker diagram shows the distribution of seedling hypocotyl length
526 values determined by the algorithm and two human experimenters. Median is
527 marked by a horizontal line inside the box, boxes depict the quartiles, and whiskers
528 extend to show the rest of the distribution. Black diamonds represent outliers.
529 Sample number at every data point is n=30.

530 **Figure 3. *Sinapis alba* hypocotyl and *Brachypodium distachyon* coleoptile**
531 **measurements by the algorithm.**
532 (a) Original images of light-grown *Sinapis alba* and *Brachypodium distachyon* plantlets
533 (left side). Image panels at the right side depict the segmentation made by the
534 algorithm. The original images also contain a millimetre paper for size scale.
535 (b) Box-and-whisker diagrams show coleoptile and hypocotyl length values determined
536 by the U-net algorithm and two human experts. Boxes depict the quartiles, whiskers
537 extend to show the rest of the distribution, median is marked by a horizontal line
538 inside the box, whereas black diamonds represent outliers. Sample number for
539 *Sinapis alba* seedlings is n=91 and for *Brachypodium distachyon* plantlets is n≥14 in
540 each light treatment.

541
542 **Figure 4. Accuracy, recall and precision metrics for the algorithm for each light**
543 **condition.**
544 Further analysis of the data what are presented in Fig. 2, Fig. 3 and Supplemental Figures
545 S2, S4, S6. Metrics were obtained by matching the plants identified by the algorithm to the
546 ground truth given by the experts. (A match is required to have at least 10% overlap
547 between the bounding boxes of the objects.) *Accuracy* is the relative accuracy of the
548 measurement defined by $1 - |M - L|/L$, where L is the ground truth length and M is the
549 measured length. The *precision* of the algorithm is defined as $TP/(TP + FP)$, where TP and
550 FP denote the number of true and false positives, respectively. A high precision implies the
551 majority of identified objects are indeed plants, not false detections. Finally, *recall* is given
552 by $TP/(TP + FN)$, where FN is the number of false negatives. The higher the recall, the more
553 plants were identified by the algorithm.
554 (a) Analysis of the data obtained on Arabidopsis seedlings. On the left side of the graph, the
555 applied growth conditions are marked: the numbers indicate light intensity in $\mu\text{mol m}^{-2} \text{s}^{-1}$,
556 LD= 12 h light/12 h dark cycles, WL±UVB= white light supplied with or without UV-B, Dark=
557 etiolated seedlings.
558 (b) The same metrics were calculated from the data obtained on *Brachypodium distachyon*
559 and *Sinapis alba* seedlings.

560
561
562 **Figure 5. Intra- and inter-expert accuracies vs the algorithm.**
563 *Intra-expert accuracy* was calculated by averaging the accuracies between the two
564 measurements from the same expert. *Inter-expert accuracy* (Expert 1 vs Expert 2) was
565 determined by comparing the first measurements of the two human experts. For
566 comparison, the accuracy of the algorithm is also presented.

567 **References**

- 568 **Ádám É, Kircher S, Liu P, Mérai Z, González-Schain N, Hörner M, Viczián A, Monte E,**
569 **Sharrock RA, Schäfer E, et al** (2013) Comparative functional analysis of full-length
570 and N-terminal fragments of phytochrome C, D and E in red light-induced signaling.
571 *New Phytol* **200**: 86–96
- 572 **Alves SC, Worland B, Thole V, Snape JW, Bevan MW, Vain P** (2009) A protocol for
573 Agrobacterium-mediated transformation of *Brachypodium distachyon* community
574 standard line Bd21. *Nat Protoc* **4**: 638–649
- 575 **Arsovski AA, Galstyan A, Guseman JM, Nemhauser JL** (2012) Photomorphogenesis.
576 *Arabidopsis Book* **10**: e0147
- 577 **Bernula P, Crocco CD, Arongaus AB, Ulm R, Nagy F, Viczián A** (2017) Expression of
578 the UVR8 photoreceptor in different tissues reveals tissue-autonomous features of UV-
579 B signalling: UVR8 signalling in different tissues. *Plant Cell Environ* **40**: 1104–1114
- 580 **Borevitz J, Neff M** (2008) Phenotypic analysis of *Arabidopsis* mutants: hypocotyl length.
581 *CSH Protoc* **2008**: db.prot4962
- 582 **Buda M, Saha A, Mazurowski MA** (2019) Association of genomic subtypes of lower-grade
583 gliomas with shape features automatically extracted by a deep learning algorithm.
584 *Comput Biol Med* **109**: 218–225
- 585 **Casal JJ, Qüesta JI** (2018) Light and temperature cues: multitasking receptors and
586 transcriptional integrators. *New Phytol* **217**: 1029–1034
- 587 **Cole B, Kay SA, Chory J** (2011) Automated analysis of hypocotyl growth dynamics during
588 shade avoidance in *Arabidopsis*. *Plant J* **65**: 991–1000
- 589 **Das D, St Onge KR, Voeselek LACJ, Pierik R, Sasidharan R** (2016) Ethylene- and
590 Shade-Induced Hypocotyl Elongation Share Transcriptome Patterns and Functional
591 Regulators. *Plant Physiol* **172**: 718–733
- 592 **Dieterle M, Thomann A, Renou J-P, Parmentier Y, Cognat V, Lemonnier G, Müller R,**
593 **Shen W-H, Kretsch T, Genschik P** (2005) Molecular and functional characterization of
594 *Arabidopsis* Cullin 3A. *Plant J* **41**: 386–399
- 595 **Fahn A** (1990) *Plant anatomy*. Pergamon
- 596 **Fankhauser C, Casal JJ** (2004) Phenotypic characterization of a photomorphogenic
597 mutant. *Plant J* **39**: 747–760
- 598 **Favory J-J, Stec A, Gruber H, Rizzini L, Oravecz A, Funk M, Albert A, Cloix C, Jenkins**
599 **GI, Oakeley EJ, et al** (2009) Interaction of COP1 and UVR8 regulates UV-B-induced
600 photomorphogenesis and stress acclimation in *Arabidopsis*. *EMBO J* **28**: 591–601
- 601 **Geirhos R, Temme CRM, Rauber J, Schütt HH, Bethge M, Wichmann FA** (2018)
602 Generalisation in humans and deep neural networks. *In* S Bengio, H Wallach, H
603 Larochelle, K Grauman, N Cesa-Bianchi, R Garnett, eds, *Advances in Neural*
604 *Information Processing Systems* 31. Curran Associates, Inc., pp 7549–7561
- 605 **Gendreau E, Traas J, Desnos T, Grandjean O, Caboche M, Höfte H** (1997) Cellular basis
606 of hypocotyl growth in *Arabidopsis thaliana*. *Plant Physiol* **114**: 295–305

- 607 **Hayashi Y, Takahashi K, Inoue S-I, Kinoshita T** (2014) Abscisic acid suppresses
608 hypocotyl elongation by dephosphorylating plasma membrane H(+)-ATPase in
609 *Arabidopsis thaliana*. *Plant Cell Physiol* **55**: 845–853
- 610 **He K, Gkioxari G, Dollar P, Girshick R** (2017) Mask R-CNN. 2017 IEEE International
611 Conference on Computer Vision (ICCV). IEEE, pp 2980–2988
- 612 **International Brachypodium Initiative** (2010) Genome sequencing and analysis of the
613 model grass *Brachypodium distachyon*. *Nature* **463**: 763–768
- 614 **Ioffe S, Szegedy C** (2015) Batch normalization: accelerating deep network training by
615 reducing internal covariate shift. Proceedings of the 32nd International Conference on
616 International Conference on Machine Learning - Volume 37. JMLR.org, pp 448–456
- 617 **Jung J-H, Domijan M, Klose C, Biswas S, Ezer D, Gao M, Khattak AK, Box MS,
618 Charoensawan V, Cortijo S, et al** (2016) Phytochromes function as thermosensors in
619 *Arabidopsis*. *Science* **354**: 886–889
- 620 **Kim BC, Tennessen DJ, Last RL** (1998) UV-B-induced photomorphogenesis in
621 *Arabidopsis thaliana*. *Plant J* **15**: 667–674
- 622 **Kingma DP, Ba J** (2014) Adam: A Method for Stochastic Optimization. arXiv [cs.LG]
- 623 **Köhler D** (1978) The Course of Ortho-Geotropic Reactions of Shoots. *Zeitschrift für*
624 *Pflanzenphysiologie* **87**: 463–467
- 625 **Lee TC, Kashyap RL, Chu CN** (1994) Building Skeleton Models via 3-D Medial Surface
626 Axis Thinning Algorithms. *CVGIP: Graphical Models and Image Processing* **56**: 462–
627 478
- 628 **Legris M, Klose C, Burgie ES, Rojas CCR, Neme M, Hiltbrunner A, Wigge PA, Schäfer
629 E, Vierstra RD, Casal JJ** (2016) Phytochrome B integrates light and temperature
630 signals in *Arabidopsis*. *Science* **354**: 897–900
- 631 **Lin C, Ahmad M, Cashmore AR** (1996) *Arabidopsis* cryptochrome 1 is a soluble protein
632 mediating blue light-dependent regulation of plant growth and development. *Plant J* **10**:
633 893–902
- 634 **Liscum E, Hangarter RP** (1991) *Arabidopsis* Mutants Lacking Blue Light-Dependent
635 Inhibition of Hypocotyl Elongation. *Plant Cell* **3**: 685–694
- 636 **Milletari F, Navab N, Ahmadi S-A** (2016) V-Net: Fully Convolutional Neural Networks for
637 Volumetric Medical Image Segmentation. 2016 Fourth International Conference on 3D
638 Vision (3DV). doi: 10.1109/3dv.2016.79
- 639 **Nagy F, Schäfer E** (2002) Phytochromes control photomorphogenesis by differentially
640 regulated, interacting signaling pathways in higher plants. *Annu Rev Plant Biol* **53**: 329–
641 355
- 642 **Namin ST, Esmailzadeh M, Najafi M, Brown TB, Borevitz JO** (2018) Deep phenotyping:
643 deep learning for temporal phenotype/genotype classification. *Plant Methods* **14**: 66
- 644 **Pepper AE, Seong-Kim M, Hebst SM, Ivey KN, Kwak SJ, Broyles DE** (2001) *shl*, a New
645 set of *Arabidopsis* mutants with exaggerated developmental responses to available red,
646 far-red, and blue light. *Plant Physiol* **127**: 295–304
- 647 **Pineda M, Pérez-Bueno ML, Barón M** (2018) Detection of Bacterial Infection in Melon

- 648 Plants by Classification Methods Based on Imaging Data. *Front Plant Sci* **9**: 164
- 649 **Pound MP, Atkinson JA, Townsend AJ, Wilson MH, Griffiths M, Jackson AS, Bulat A,**
650 **Tzimiropoulos G, Wells DM, Murchie EH, et al** (2017) Deep machine learning
651 provides state-of-the-art performance in image-based plant phenotyping. *GigaScience*.
652 doi: 10.1093/gigascience/gix083
- 653 **Procko C, Crenshaw CM, Ljung K, Noel JP, Chory J** (2014) Cotyledon-Generated Auxin
654 Is Required for Shade-Induced Hypocotyl Growth in *Brassica rapa*. *Plant Physiol* **165**:
655 1285–1301
- 656 **Ramcharan A, McCloskey P, Baranowski K, Mbilinyi N, Mrisho L, Ndalaha M, Legg J,**
657 **Hughes DP** (2019) A Mobile-Based Deep Learning Model for Cassava Disease
658 Diagnosis. *Front Plant Sci* **10**: 272
- 659 **Ronneberger O, Fischer P, Brox T** (2015) U-Net: Convolutional Networks for Biomedical
660 Image Segmentation. *Medical Image Computing and Computer-Assisted Intervention –*
661 *MICCAI 2015*. Springer International Publishing, pp 234–241
- 662 **Sangster TA, Salathia N, Undurraga S, Milo R, Schellenberg K, Lindquist S, Queitsch**
663 **C** (2008) HSP90 affects the expression of genetic variation and developmental stability
664 in quantitative traits. *Proc Natl Acad Sci U S A* **105**: 2963–2968
- 665 **Schindelin J, Arganda-Carreras I, Frise E, Kaynig V, Longair M, Pietzsch T, Preibisch**
666 **S, Rueden C, Saalfeld S, Schmid B, et al** (2012) Fiji: an open-source platform for
667 biological-image analysis. *Nat Methods* **9**: 676–682
- 668 **Scholthof K-BG, Irigoyen S, Catalan P, Mandadi KK** (2018) Brachypodium: A Monocot
669 Grass Model Genus for Plant Biology. *Plant Cell* **30**: 1673–1694
- 670 **Schopfer P, Oelze-Karow H** (1971) [Demonstration of a threshold regulation by
671 phytochrome in the photomodulation of longitudinal growth of the hypocotyl of mustard
672 seedlings (*Sinapis alba* L.)]. *Planta* **100**: 167–180
- 673 **Singh AK, Ganapathysubramanian B, Sarkar S, Singh A** (2018) Deep Learning for Plant
674 Stress Phenotyping: Trends and Future Perspectives. *Trends Plant Sci* **23**: 883–898
- 675 **Soga K, Yamazaki C, Kamada M, Tanigawa N, Kasahara H, Yano S, Kojo KH, Kutsuna**
676 **N, Kato T, Hashimoto T, et al** (2018) Modification of growth anisotropy and cortical
677 microtubule dynamics in *Arabidopsis* hypocotyls grown under microgravity conditions in
678 space. *Physiol Plant* **162**: 135–144
- 679 **Spalding EP, Miller ND** (2013) Image analysis is driving a renaissance in growth
680 measurement. *Current Opinion in Plant Biology* **16**: 100–104
- 681 **Sudre CH, Li W, Vercauteren T, Ourselin S, Jorge Cardoso M** (2017) Generalised Dice
682 Overlap as a Deep Learning Loss Function for Highly Unbalanced Segmentations.
683 *Deep Learning in Medical Image Analysis and Multimodal Learning for Clinical Decision*
684 *Support* 240–248
- 685 **Vandenbussche F, Verbelen J-P, Van Der Straeten D** (2005) Of light and length:
686 regulation of hypocotyl growth in *Arabidopsis*. *Bioessays* **27**: 275–284
- 687 **van der Walt S, Schönberger JL, Nunez-Iglesias J, Boulogne F, Warner JD, Yager N,**
688 **Gouillart E, Yu T, scikit-image contributors** (2014) scikit-image: image processing in
689 Python. *PeerJ* **2**: e453

- 690 **Wang L, Uilecan IV, Assadi AH, Kozmik CA, Spalding EP** (2009) HYPOTrace: image
691 analysis software for measuring hypocotyl growth and shape demonstrated on
692 Arabidopsis seedlings undergoing photomorphogenesis. *Plant Physiol* **149**: 1632–1637
- 693 **Wildermann A, Drumm H, Schäfer E, Mohr H** (1978a) Control by light of hypocotyl growth
694 in de-etiolated mustard seedlings : I. Phytochrome as the only photoreceptor pigment.
695 *Planta* **141**: 211–216
- 696 **Wildermann A, Drumm H, Schäfer E, Mohr H** (1978b) Control by light of hypocotyl growth
697 in de-etiolated mustard seedlings : II. Sensitivity for newly-formed phytochrome after a
698 light to dark transtition. *Planta* **141**: 217–223
- 699 **Young JC, Liscum E, Hangarter RP** (1992) Spectral-dependence of light-inhibited
700 hypocotyl elongation in photomorphogenic mutants of Arabidopsis: evidence for a UV-A
701 photosensor. *Planta* **188**: 106–114
- 702

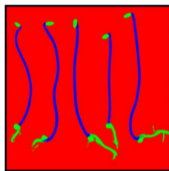
A

original

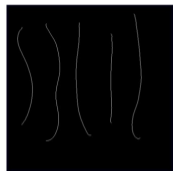
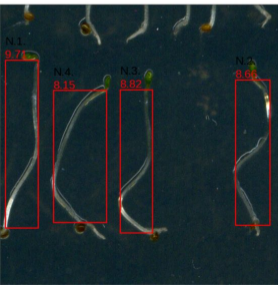


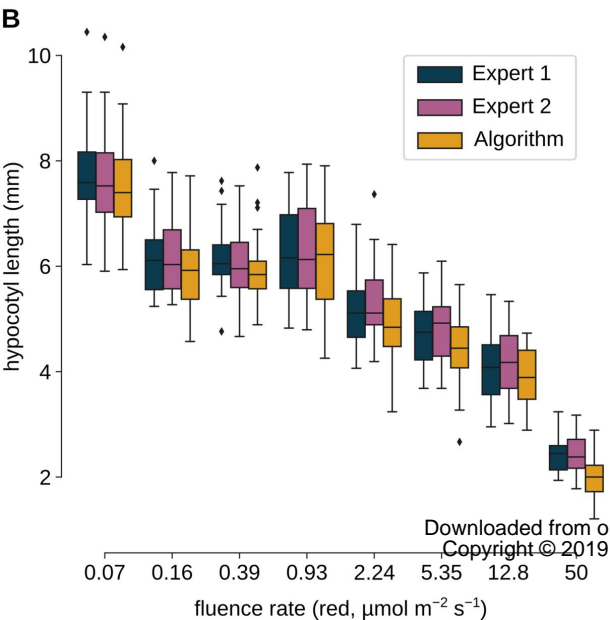
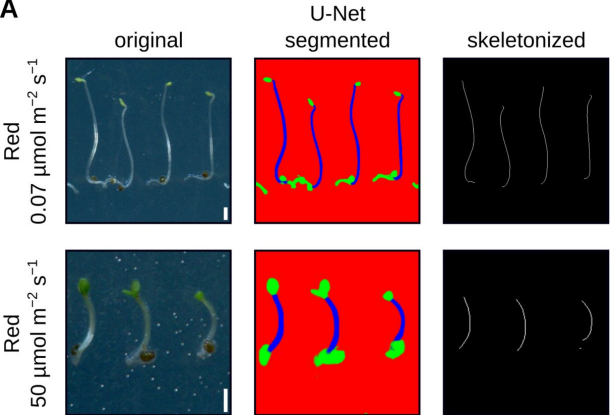
U-Net

segmentation



skeletonization

**B**Downloaded from c
Copyright © 2019



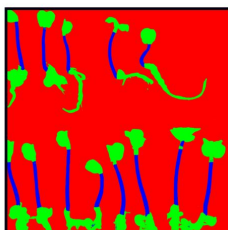
A

original

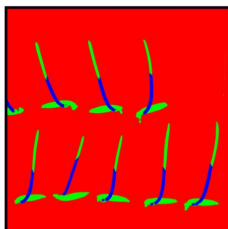
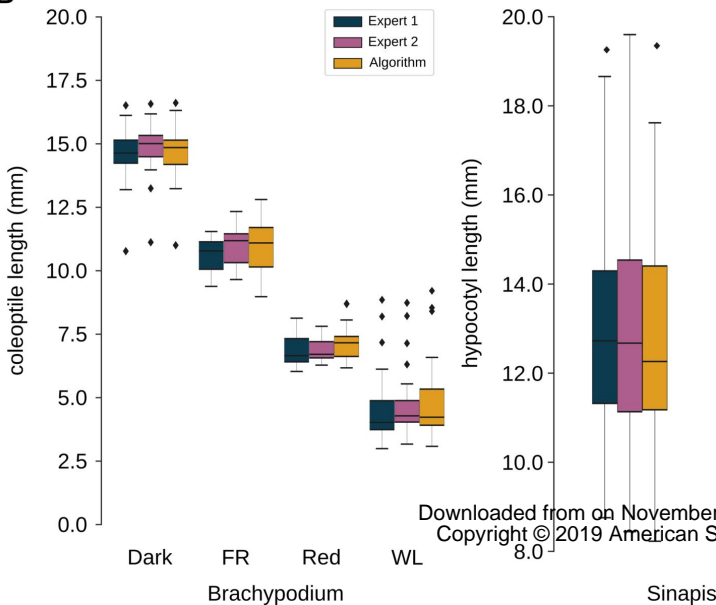
U-Net

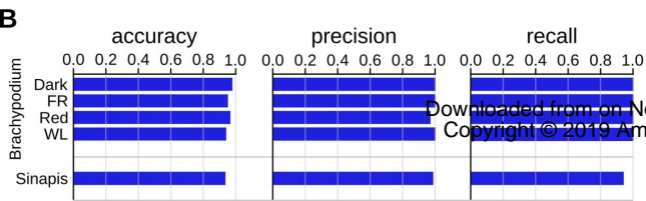
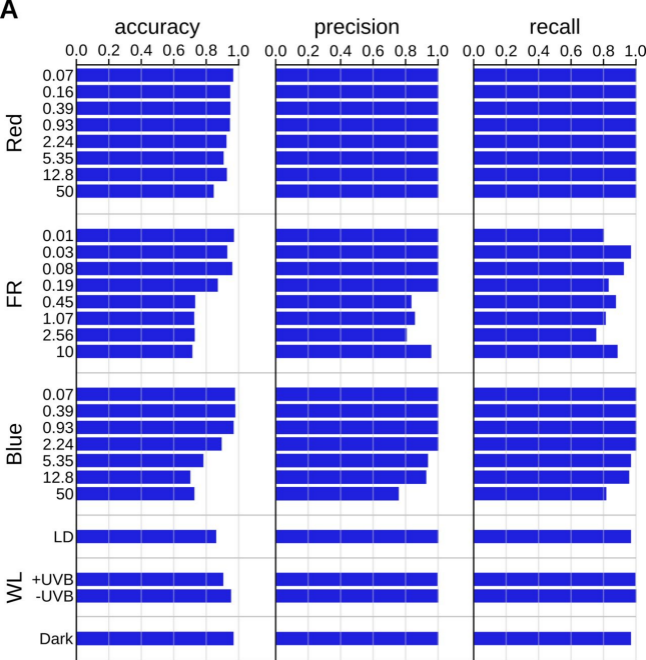
segmented

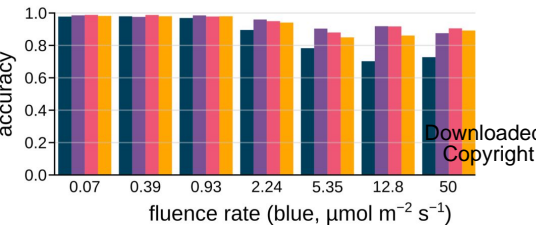
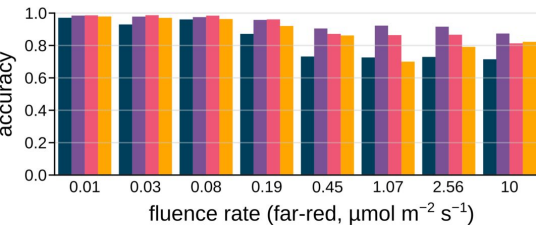
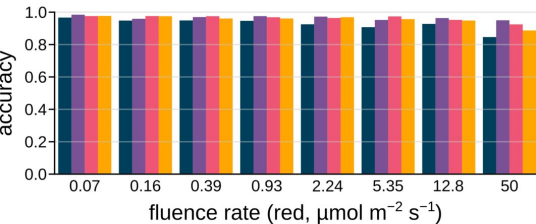
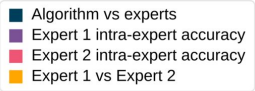
Sinapis



Brachypodium

**B**





Parsed Citations

Ádám É, Kircher S, Liu P, Mérai Z, González-Schain N, Hörner M, Viczián A, Monte E, Sharrock RA, Schäfer E, et al (2013) Comparative functional analysis of full-length and N-terminal fragments of phytochrome C, D and E in red light-induced signaling. *New Phytol* 200: 86–96

Pubmed: [Author and Title](#)

Google Scholar: [Author Only](#) [Title Only](#) [Author and Title](#)

Alves SC, Worland B, Thole V, Snape JW, Bevan MW, Vain P (2009) A protocol for *Agrobacterium*-mediated transformation of *Brachypodium distachyon* community standard line Bd21. *Nat Protoc* 4: 638–649

Pubmed: [Author and Title](#)

Google Scholar: [Author Only](#) [Title Only](#) [Author and Title](#)

Arsovski AA, Galstyan A, Guseman JM, Nemhauser JL (2012) Photomorphogenesis. *Arabidopsis Book* 10: e0147

Pubmed: [Author and Title](#)

Google Scholar: [Author Only](#) [Title Only](#) [Author and Title](#)

Bernula P, Crocco CD, Arongaus AB, Ulm R, Nagy F, Viczián A (2017) Expression of the UVR8 photoreceptor in different tissues reveals tissue-autonomous features of UV-B signalling: UVR8 signalling in different tissues. *Plant Cell Environ* 40: 1104–1114

Pubmed: [Author and Title](#)

Google Scholar: [Author Only](#) [Title Only](#) [Author and Title](#)

Borevitz J, Neff M (2008) Phenotypic analysis of *Arabidopsis* mutants: hypocotyl length. *CSH Protoc* 2008: db.prot4962

Pubmed: [Author and Title](#)

Google Scholar: [Author Only](#) [Title Only](#) [Author and Title](#)

Buda M, Saha A, Mazurowski MA (2019) Association of genomic subtypes of lower-grade gliomas with shape features automatically extracted by a deep learning algorithm. *Comput Biol Med* 109: 218–225

Pubmed: [Author and Title](#)

Google Scholar: [Author Only](#) [Title Only](#) [Author and Title](#)

Casal JJ, Qüesta JI (2018) Light and temperature cues: multitasking receptors and transcriptional integrators. *New Phytol* 217: 1029–1034

Pubmed: [Author and Title](#)

Google Scholar: [Author Only](#) [Title Only](#) [Author and Title](#)

Cole B, Kay SA, Chory J (2011) Automated analysis of hypocotyl growth dynamics during shade avoidance in *Arabidopsis*. *Plant J* 65: 991–1000

Pubmed: [Author and Title](#)

Google Scholar: [Author Only](#) [Title Only](#) [Author and Title](#)

Das D, St Onge KR, Voeselek LACJ, Pierik R, Sasidharan R (2016) Ethylene- and Shade-Induced Hypocotyl Elongation Share Transcriptome Patterns and Functional Regulators. *Plant Physiol* 172: 718–733

Pubmed: [Author and Title](#)

Google Scholar: [Author Only](#) [Title Only](#) [Author and Title](#)

Dieterle M, Thomann A, Renou J-P, Parmentier Y, Cognat V, Lemonnier G, Müller R, Shen W-H, Kretsch T, Genschik P (2005) Molecular and functional characterization of *Arabidopsis* Cullin 3A. *Plant J* 41: 386–399

Pubmed: [Author and Title](#)

Google Scholar: [Author Only](#) [Title Only](#) [Author and Title](#)

Fahn A (1990) *Plant anatomy*. Pergamon

Pubmed: [Author and Title](#)

Google Scholar: [Author Only](#) [Title Only](#) [Author and Title](#)

Fankhauser C, Casal JJ (2004) Phenotypic characterization of a photomorphogenic mutant. *Plant J* 39: 747–760

Pubmed: [Author and Title](#)

Google Scholar: [Author Only](#) [Title Only](#) [Author and Title](#)

Favory J-J, Stec A, Gruber H, Rizzini L, Oravec A, Funk M, Albert A, Cloix C, Jenkins GI, Oakeley EJ, et al (2009) Interaction of COP1 and UVR8 regulates UV-B-induced photomorphogenesis and stress acclimation in *Arabidopsis*. *EMBO J* 28: 591–601

Pubmed: [Author and Title](#)

Google Scholar: [Author Only](#) [Title Only](#) [Author and Title](#)

Geirhos R, Temme CRM, Rauber J, Schütt HH, Bethge M, Wichmann FA (2018) Generalisation in humans and deep neural networks. In S Bengio, H Wallach, H Larochelle, K Grauman, N Cesa-Bianchi, R Garnett, eds, *Advances in Neural Information Processing Systems* 31. Curran Associates, Inc., pp 7549–7561

Pubmed: [Author and Title](#)

Google Scholar: [Author Only](#) [Title Only](#) [Author and Title](#)

Gendreau E, Traas J, Desnos T, Grandjean O, Caboche M, Höfte H (1997) Cellular basis of hypocotyl growth in *Arabidopsis*

Downloaded from on November 21, 2019 - Published by www.plantphysiol.org

Copyright © 2019 American Society of Plant Biologists. All rights reserved.

thaliana. Plant Physiol 114: 295–305

Pubmed: [Author and Title](#)

Google Scholar: [Author Only](#) [Title Only](#) [Author and Title](#)

Hayashi Y, Takahashi K, Inoue S-I, Kinoshita T (2014) Abscisic acid suppresses hypocotyl elongation by dephosphorylating plasma membrane H(+)-ATPase in Arabidopsis thaliana. Plant Cell Physiol 55: 845–853

Pubmed: [Author and Title](#)

Google Scholar: [Author Only](#) [Title Only](#) [Author and Title](#)

He K, Gkioxari G, Dollar P, Girshick R (2017) Mask R-CNN. 2017 IEEE International Conference on Computer Vision (ICCV). IEEE, pp 2980–2988

Pubmed: [Author and Title](#)

Google Scholar: [Author Only](#) [Title Only](#) [Author and Title](#)

International Brachypodium Initiative (2010) Genome sequencing and analysis of the model grass Brachypodium distachyon. Nature 463: 763–768

Pubmed: [Author and Title](#)

Google Scholar: [Author Only](#) [Title Only](#) [Author and Title](#)

Ioffe S, Szegedy C (2015) Batch normalization: accelerating deep network training by reducing internal covariate shift. Proceedings of the 32nd International Conference on International Conference on Machine Learning - Volume 37. JMLR.org, pp 448–456

Pubmed: [Author and Title](#)

Google Scholar: [Author Only](#) [Title Only](#) [Author and Title](#)

Jung J-H, Domijan M, Klose C, Biswas S, Ezer D, Gao M, Khattak AK, Box MS, Charoensawan V, Cortijo S, et al (2016) Phytochromes function as thermosensors in Arabidopsis. Science 354: 886–889

Pubmed: [Author and Title](#)

Google Scholar: [Author Only](#) [Title Only](#) [Author and Title](#)

Kim BC, Tennessen DJ, Last RL (1998) UV-B-induced photomorphogenesis in Arabidopsis thaliana. Plant J 15: 667–674

Pubmed: [Author and Title](#)

Google Scholar: [Author Only](#) [Title Only](#) [Author and Title](#)

Kingma DP, Ba J (2014) Adam: A Method for Stochastic Optimization. arXiv [cs.LG]

Pubmed: [Author and Title](#)

Google Scholar: [Author Only](#) [Title Only](#) [Author and Title](#)

Köhler D (1978) The Course of Ortho-Geotropic Reactions of Shoots. Zeitschrift für Pflanzenphysiologie 87: 463–467

Pubmed: [Author and Title](#)

Google Scholar: [Author Only](#) [Title Only](#) [Author and Title](#)

Lee TC, Kashyap RL, Chu CN (1994) Building Skeleton Models via 3-D Medial Surface Axis Thinning Algorithms. CVGIP: Graphical Models and Image Processing 56: 462–478

Pubmed: [Author and Title](#)

Google Scholar: [Author Only](#) [Title Only](#) [Author and Title](#)

Legris M, Klose C, Burgie ES, Rojas CCR, Neme M, Hiltbrunner A, Wigge PA, Schäfer E, Vierstra RD, Casal JJ (2016) Phytochrome B integrates light and temperature signals in Arabidopsis. Science 354: 897–900

Pubmed: [Author and Title](#)

Google Scholar: [Author Only](#) [Title Only](#) [Author and Title](#)

Lin C, Ahmad M, Cashmore AR (1996) Arabidopsis cryptochrome 1 is a soluble protein mediating blue light-dependent regulation of plant growth and development. Plant J 10: 893–902

Pubmed: [Author and Title](#)

Google Scholar: [Author Only](#) [Title Only](#) [Author and Title](#)

Liscum E, Hangarter RP (1991) Arabidopsis Mutants Lacking Blue Light-Dependent Inhibition of Hypocotyl Elongation. Plant Cell 3: 685–694

Pubmed: [Author and Title](#)

Google Scholar: [Author Only](#) [Title Only](#) [Author and Title](#)

Milletari F, Navab N, Ahmadi S-A (2016) V-Net: Fully Convolutional Neural Networks for Volumetric Medical Image Segmentation. 2016 Fourth International Conference on 3D Vision (3DV). doi: 10.1109/3dv.2016.79

Pubmed: [Author and Title](#)

Google Scholar: [Author Only](#) [Title Only](#) [Author and Title](#)

Nagy F, Schäfer E (2002) Phytochromes control photomorphogenesis by differentially regulated, interacting signaling pathways in higher plants. Annu Rev Plant Biol 53: 329–355

Pubmed: [Author and Title](#)

Google Scholar: [Author Only](#) [Title Only](#) [Author and Title](#)

Namin ST, Esmailzadeh M, Najafi M, Brown TB, Borevitz JO (2018) Deep phenotyping: deep learning for temporal phenotype/genotype classification. Plant Methods 14: 66

Pubmed: [Author and Title](#)

Google Scholar: [Author Only](#) [Title Only](#) [Author and Title](#)

Pepper AE, Seong-Kim M, Hebst SM, Ivey KN, Kwak SJ, Broyles DE (2001) shl, a New set of Arabidopsis mutants with exaggerated developmental responses to available red, far-red, and blue light. Plant Physiol 127: 295–304

Pubmed: [Author and Title](#)

Google Scholar: [Author Only](#) [Title Only](#) [Author and Title](#)

Pineda M, Pérez-Bueno ML, Barón M (2018) Detection of Bacterial Infection in Melon Plants by Classification Methods Based on Imaging Data. Front Plant Sci 9: 164

Pubmed: [Author and Title](#)

Google Scholar: [Author Only](#) [Title Only](#) [Author and Title](#)

Pound MP, Atkinson JA, Townsend AJ, Wilson MH, Griffiths M, Jackson AS, Bulat A, Tzimiropoulos G, Wells DM, Murchie EH, et al (2017) Deep machine learning provides state-of-the-art performance in image-based plant phenotyping. GigaScience. doi: 10.1093/gigascience/gix083

Pubmed: [Author and Title](#)

Google Scholar: [Author Only](#) [Title Only](#) [Author and Title](#)

Procko C, Crenshaw CM, Ljung K, Noel JP, Chory J (2014) Cotyledon-Generated Auxin Is Required for Shade-Induced Hypocotyl Growth in Brassica rapa. Plant Physiol 165: 1285–1301

Pubmed: [Author and Title](#)

Google Scholar: [Author Only](#) [Title Only](#) [Author and Title](#)

Ramcharan A, McCloskey P, Baranowski K, Mbilinyi N, Mrisho L, Ndalahwa M, Legg J, Hughes DP (2019) A Mobile-Based Deep Learning Model for Cassava Disease Diagnosis. Front Plant Sci 10: 272

Pubmed: [Author and Title](#)

Google Scholar: [Author Only](#) [Title Only](#) [Author and Title](#)

Ronneberger O, Fischer P, Brox T (2015) U-Net: Convolutional Networks for Biomedical Image Segmentation. Medical Image Computing and Computer-Assisted Intervention – MICCAI 2015. Springer International Publishing, pp 234–241

Pubmed: [Author and Title](#)

Google Scholar: [Author Only](#) [Title Only](#) [Author and Title](#)

Sangster TA, Salathia N, Undurraga S, Milo R, Schellenberg K, Lindquist S, Queitsch C (2008) HSP90 affects the expression of genetic variation and developmental stability in quantitative traits. Proc Natl Acad Sci U S A 105: 2963–2968

Pubmed: [Author and Title](#)

Google Scholar: [Author Only](#) [Title Only](#) [Author and Title](#)

Schindelin J, Arganda-Carreras I, Frise E, Kaynig V, Longair M, Pietzsch T, Preibisch S, Rueden C, Saalfeld S, Schmid B, et al (2012) Fiji: an open-source platform for biological-image analysis. Nat Methods 9: 676–682

Pubmed: [Author and Title](#)

Google Scholar: [Author Only](#) [Title Only](#) [Author and Title](#)

Scholthof K-BG, Irigoyen S, Catalan P, Mandadi KK (2018) Brachypodium: A Monocot Grass Model Genus for Plant Biology. Plant Cell 30: 1673–1694

Pubmed: [Author and Title](#)

Google Scholar: [Author Only](#) [Title Only](#) [Author and Title](#)

Schopfer P, Oelze-Karow H (1971) [Demonstration of a threshold regulation by phytochrome in the photomodulation of longitudinal growth of the hypocotyl of mustard seedlings (Sinapis alba L.)]. Planta 100: 167–180

Pubmed: [Author and Title](#)

Google Scholar: [Author Only](#) [Title Only](#) [Author and Title](#)

Singh AK, Ganapathysubramanian B, Sarkar S, Singh A (2018) Deep Learning for Plant Stress Phenotyping: Trends and Future Perspectives. Trends Plant Sci 23: 883–898

Pubmed: [Author and Title](#)

Google Scholar: [Author Only](#) [Title Only](#) [Author and Title](#)

Soga K, Yamazaki C, Kamada M, Tanigawa N, Kasahara H, Yano S, Kojo KH, Kutsuna N, Kato T, Hashimoto T, et al (2018) Modification of growth anisotropy and cortical microtubule dynamics in Arabidopsis hypocotyls grown under microgravity conditions in space. Physiol Plant 162: 135–144

Pubmed: [Author and Title](#)

Google Scholar: [Author Only](#) [Title Only](#) [Author and Title](#)

Spalding EP, Miller ND (2013) Image analysis is driving a renaissance in growth measurement. Current Opinion in Plant Biology 16: 100–104

Pubmed: [Author and Title](#)

Google Scholar: [Author Only](#) [Title Only](#) [Author and Title](#)

Sudre CH, Li W, Vercauteren T, Ourselin S, Jorge Cardoso M (2017) Generalised Dice Overlap as a Deep Learning Loss Function for Highly Unbalanced Segmentations. Deep Learning in Medical Image Analysis and Multimodal Learning for Clinical Decision Support 240–248

Pubmed: [Author and Title](#)

Google Scholar: [Author Only](#) [Title Only](#) [Author and Title](#)

Vandenbussche F, Verbelen J-P, Van Der Straeten D (2005) Of light and length: regulation of hypocotyl growth in Arabidopsis. Bioessays 27: 275–284

Pubmed: [Author and Title](#)

Google Scholar: [Author Only](#) [Title Only](#) [Author and Title](#)

van der Walt S, Schönberger JL, Nunez-Iglesias J, Boulogne F, Warner JD, Yager N, Gouillart E, Yu T, scikit-image contributors (2014) scikit-image: image processing in Python. PeerJ 2: e453

Pubmed: [Author and Title](#)

Google Scholar: [Author Only](#) [Title Only](#) [Author and Title](#)

Wang L, Uilecan IV, Assadi AH, Kozmik CA, Spalding EP (2009) HYPOTrace: image analysis software for measuring hypocotyl growth and shape demonstrated on Arabidopsis seedlings undergoing photomorphogenesis. Plant Physiol 149: 1632–1637

Pubmed: [Author and Title](#)

Google Scholar: [Author Only](#) [Title Only](#) [Author and Title](#)

Wildermann A, Drumm H, Schäfer E, Mohr H (1978a) Control by light of hypocotyl growth in de-etiolated mustard seedlings : I. Phytochrome as the only photoreceptor pigment. Planta 141: 211–216

Pubmed: [Author and Title](#)

Google Scholar: [Author Only](#) [Title Only](#) [Author and Title](#)

Wildermann A, Drumm H, Schäfer E, Mohr H (1978b) Control by light of hypocotyl growth in de-etiolated mustard seedlings : II. Sensitivity for newly-formed phytochrome after a light to dark transtition. Planta 141: 217–223

Pubmed: [Author and Title](#)

Google Scholar: [Author Only](#) [Title Only](#) [Author and Title](#)

Young JC, Liscum E, Hangarter RP (1992) Spectral-dependence of light-inhibited hypocotyl elongation in photomorphogenic mutants of Arabidopsis: evidence for a UV-A photosensor. Planta 188: 106–114

Pubmed: [Author and Title](#)

Google Scholar: [Author Only](#) [Title Only](#) [Author and Title](#)